Thermal radiative properties of electron-beam-melted and mechanically alloyed V-4Cr-4Ti based alloys between 200 and 750 ºC

T. Echániz[a,*], I. González de Arrieta[b], R. Fuente[a], I. Urcelay-Olabarria[b], J.M. Igartua[b], N. de la Pinta[c], W. Ran[d], H. Fu[d], J. Chen[d], P.F. Zheng[d], M.J. Tello[c,e], G.A. López[b]

a) Applied Mathematics, University of the Basque Country UPV/EHU, Plaza Ingeniero Torres Quevedo 1, Bilbao, 48013, Spain

b) Applied Physics II, University of the Basque Country UPV/EHU, Leioa, 48940, Spain

c) Condensed Matter Physics, University of the Basque Country UPV/EHU, Leioa, 48940, Spain

d) Fusion Materials Division, Southwestern Institute of Physics, Chengdu, Sichuan, P.R. China

e) Instituto de Síntesis y Estudio de Materiales, University of the Basque Country UPV/EHU, 48080 Bilbao, Spain

*Corresponding author: telmo.echaniz@ehu.es

Abstract

The directional spectral emissivities of two V-4Cr-4Ti family alloys, candidate structural materials for fusion first wall/blanket applications, were measured between 200 ºC and their working temperatures (700−750 ºC), with and without a high-temperature treatment. Besides showing the typical metallic behavior, an increase in the emissivity after the heat treatment (1000-1200 ºC) was observed in both alloys. This has been attributed to several microstructural changes, which show the important role of microstructure in the thermal radiative properties of these alloys. In order to explain these mechanisms, the samples were analyzed using electron microscopy and X-ray diffraction. These measurements revealed differences in grain size, composition of the main phase and amount and distribution of dispersed secondary phases. X-ray diffraction and X-ray photoelectron spectroscopy were also used in order to check the extent of oxygen penetration. The results of directional spectral emissivity measurements were integrated to calculate the total hemispherical emissivity, the key heat transfer parameter in the high-temperature high-vacuum environments of fusion reactors. It is observed that the strategy of mechanical alloying with oxide and carbide dispersion to improve the mechanical properties also translates into an enhancement of the radiative refrigerating capability of these alloys.

Keywords: vanadium alloys, emissivity, heat transfer, fusion energy, radiative properties, thermophysical properties

1 Introduction

Vanadium alloys are candidate structural materials for the first wall/blanket in fusion reactors, mainly due to the design requirements of low-activation materials [1, 2]. As a result of its superior nuclear performance and high-temperature mechanical properties, V-4Cr-4Ti has been selected as the leading candidate for liquid lithium self-cooled blankets in fusion reactors [3-5]. Among the requirements demanded for the materials used in the first wall/blanket environment, the most important ones are the conversion of the kinetic energy of neutrons into heat and the extraction of that heat to generate power [6]. Therefore, accurate data of the radiative properties at working temperatures becomes necessary, among other information, as input parameters for numerical simulation (to optimize thermal processes calculating radiative heat transfer), for non-contact temperature measurements and for the accurate use of infrared thermography as a non-destructive testing technique [7-10]. This is particularly important for systems that are used under vacuum conditions, such as nuclear reactors, where heat transfer occurs mainly by radiation. These facts justify the effort that is being made in the measurements of infrared emissivity of candidate materials for fusion and fission reactors [11-14].

No data on the radiative properties of vanadium-based alloys has been found in the literature. Only some spectral emissivity measurements below 1 μm (where only 1% of the total thermal radiation is emitted below 1000 ºC) and total hemispherical emissivity data determined by calorimetric methods were found for pure vanadium [15-18]. In any case, data reported for pure metals cannot generally be extrapolated to alloys since optical and radiative properties depend on the presence of alloying elements, secondary phases, precipitates, etcetera [19,20]. Overall, this highlights the lack of emissivity data in vanadium-based materials and the need to perform further studies on their thermal radiative properties.

Taking into account the interest of V-based alloys for their application in nuclear fusion reactors, the present contribution presents the first complete study on the thermal radiative properties for two of these alloys: V-4Cr-4Ti and V-4Cr-4Ti-1.8Y-0.4Ti$_3$SiC$_2$ (mass %). These data can be useful for several applications concerning the deployment of these materials in fusion reactors, such as calculations of heat flow, as well as *in situ* thermography for non-contact temperature measurements and non-destructive testing purposes.

2 Experimental

The samples measured covered two alloys of the V-4Cr-4Ti family: the base alloy and a special one with additional 1.8% Y and 0.4%Ti$_3$SiC$_2$. Two samples of the former

composition were synthesized by electron beam melting and processed by hot rolling at 900-1050 ºC, cold rolling at room temperature and annealing at 1020 ºC for 2 hours to remove inner stress. Two samples of the latter were synthesized by mechanical alloying and eventually processed by hot isostatic pressing under 150 MPa at 1100 ºC for 2.5 hours. A complete study of the microstructure of both alloys has been done elsewhere [21-23]. Minor amounts of C and O as impurities were present in the starting materials. Nevertheless, in order to investigate the thermal stability of the microstructure and its effect in the thermal radiative properties, one sample of each alloy was heat treated inside an alumina crucible placed on an alumina tube under vacuum performed by a turbomolecular pump ($4 \cdot 10^{-5}$ mbar). The V-4Cr-4Ti alloy (EBM-HT) was heat treated for 2 hours at 1000 ºC, whereas the V-4Cr-4Ti-1.8Y-0.4 Ti_3SiC_2 alloy (MA-HT) was treated for 2 hours at 1200 ºC. A Zr foil was used as an oxygen getter in both cases. Table 1 shows the characteristics of each sample and the acronyms used for each sample in this paper. Samples were mechanically polished with P800 SiC paper to ensure a repeatable surface since emissivity values can be strongly dependent on the surface roughness, which was measured with a mechanical profilometer (Mitutoyo SJ201 roughness tester). The results are shown in Table 2. The observed average roughness is well below the wavelengths studied in these emissivity measurements and therefore should not have significant effects in them.

Table 1 Summary of the compositions, heat treatments and acronyms are displayed.

Sample	Synthesis	Heat Treatment	Acronym
V-4Cr-4Ti	Electron Beam Melting	No	EBM
V-4Cr-4Ti-1.8Y-0.4Ti_3SiC_2	Mechanical Alloying	No	MA
V-4Cr-4Ti	Electron Beam Melting	2 h (1000 ºC)	EBM-HT
V-4Cr-4Ti-1.8Y-0.4Ti_3SiC_2	Mechanical Alloying	2 h (1200 ºC)	MA-HT

Table 2 Surface roughness of the samples. R_a stands for the average roughness, R_q for the root-mean-square roughness, R_z for the average height of the profile peaks and R_t for the absolute highest peak value.

Sample	R_a (μm)	R_q (μm)	R_z (μm)	R_t (μm)
EBM	0.11	0.14	0.85	1.34
MA	0.16	0.24	1.55	2.14
EBM-HT	0.09	0.11	0.76	0.84
MA-HT	0.14	0.18	1.16	1.69

The emissivity measurements were made using the high-accuracy HAIRL radiometer [24], which allows directional emissivity measurements in a controlled atmosphere at temperatures up to 1000 ºC. The sample temperature was measured by two K-type thermocouples located in holes machined in the material. The measurement method was the modified *blacksur* method [25] and the radiometer response was calibrated by a high-temperature blackbody and a room-temperature high-emissivity coating [26]. Measurements are made avoiding normal incidence to get rid of spurious radiation, with normal spectral emissivity values obtained from 10º measurements, as the emissivity does not evolve in metals between 0 and 20º [27]. The combined standard uncertainty was studied elsewhere [28] and it is displayed with shades in the spectral emissivity data.

The sample chamber reaches a base pressure of $1.5 \cdot 10^{-4}$ mbar. In the case of V-based alloys this vacuum level might not be enough to entirely avoid high temperature oxidation and oxygen diffusion in the metallic matrix [29]. To minimize this effect all measurements were performed using a Zr foil as an oxygen getter.

Complementary characterization techniques have been used to understand the microscopic mechanisms responsible for the evolution of the thermal radiative properties of these alloys. Optical and scanning electron microscopies (SEM) were used to investigate the microstructure. Electron back-scattered diffraction (EBSD) measurements were done in a TESCAN Mira3 XMH field emission gun microscope equipped with an Oxford Instruments Aztec system and operated at 20 kV using a step size of 0.2 μm. Misorientation maps and grain size were obtained taking into account a 15º misorientation threshold for high-angle grain boundaries. Transmission electron microscopy (TEM) was employed to study the size of the precipitates. X-ray diffraction patterns were acquired using Cu K_α radiation in Bragg-Brentano geometry with an angle step of 0.02 º in an X'Pert-Pro diffractometer. To characterize the outermost layer of the samples, X-ray photoelectron spectroscopy (XPS) depth profiles were done in a SPECS system equipped with a Phoibos 150 1D-DLD analyzer and a monochromatic Al K_α source. The oxide layer was determined using a Ta_2O_5 reference with Ar^+ sputtering. The ion energies and current applied were 3000 and 5000-eV and 10-mA, respectively.

3 Results and Discussion

3. 1 Microstructural characterization

To support the upcoming discussions on the emissivity data obtained from both samples in two different states, a complementary microstructural characterization is provided in this section. Figure 1a shows an optical micrograph of the EBM sample, with equiaxed grains of about 40 μm [22]. Only a very slight coarsening/grain growth of the Ti/Cr-carbides present in this sample and the complete solution of the metallic elements are expected upon heat treatment at 1000 ºC for 2 h applied in the current work, but with no change in the grain size of the matrix [22]. The MA and MA-HT samples (Figures 1b and 1c respectively) were analyzed by SEM and by EBSD. It was observed that in the MA sample there is bimodal grain size distribution (Figures 1b and 1d) with some large grains together with a large population of fine grains. After the heat treatment, growth in the average size of grains is observed, together with a homogenization of the size distribution (no large grains). Then, a transmission electron bright field image of the MA-HT sample is presented in Figure 1e. As reported for another set of V-4Cr-4Ti nanoparticle strengthened alloys, the mean size of the precipitates and their number density increased upon heat treatment [23].
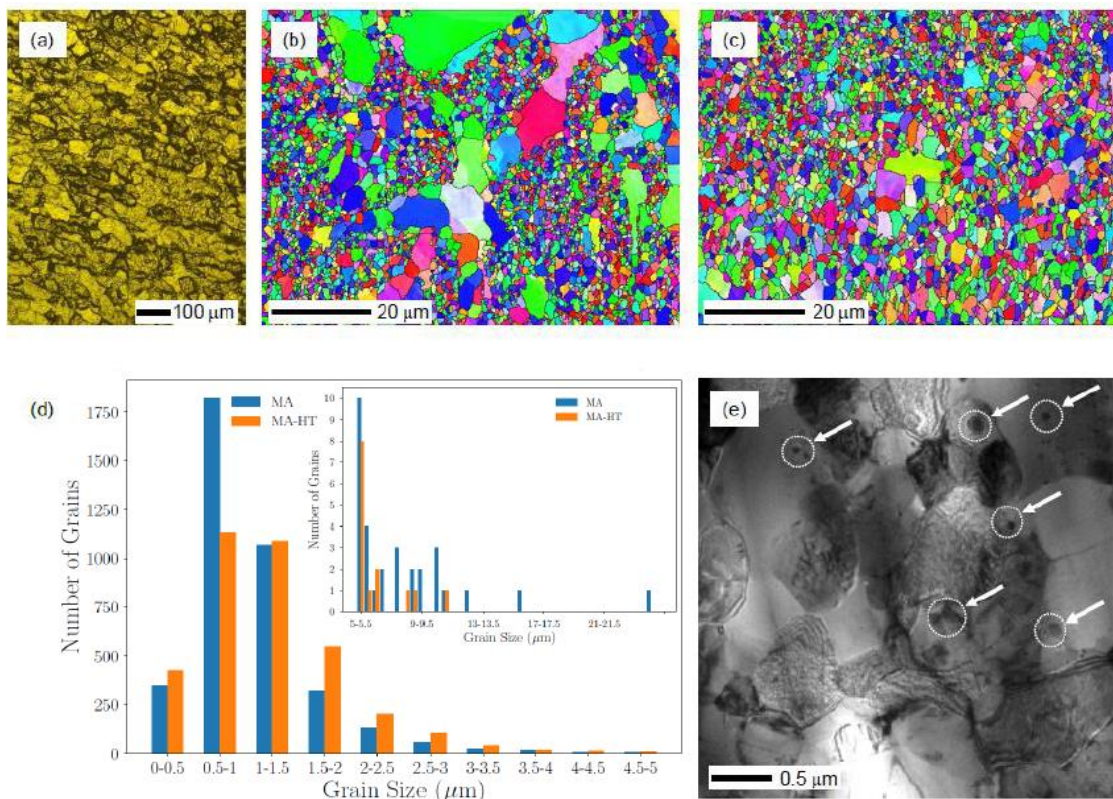
Figure 1 (a) Optical micrograph of the EBM sample. EBSD misorientation maps for (b) the MA sample and (c) the MA-HT sample. For the two samples, (d) grain size distribution was determined taking into account a 15º misorientation threshold for high-angle grain boundaries. In the inset the low number of large grains is shown. e) Transmission electron bright field image of the MA-HT sample showing the presence of coarsened precipitates due to the heat treatment at 1200 ºC for 2 h.

X-ray diffraction (XRD) patterns obtained for all the samples are depicted in Figure 2. On the one hand, in the case of the EBM and EBM-HT samples, the reflections corresponding to the metallic solid-solutions were the most intense, although a very small amount of precipitates (mainly carbides) was also observed, being in agreement with a previous work [22]. In the case of the EBM sample, reflections corresponding to the (V) solid-solution together with those from two other BCC solutions were indexed, which after the heat treatment merged in a single (V) solid-solution in the EBM-HT sample. Besides, there was a slight increase in the intensity of the carbides reflections upon heat treatment. On the other hand, for both MA and MA-HT samples, in addition to the reflections of the (V) matrix, those corresponding to the nanoparticle reinforcements (primarily Y_2O_3 coming from the oxidation of the added Y) are also present. In the case of the MA-HT sample, the intensity of Y_2O_3 reflections, as expected, is higher [23]. The occurrence of precipitates that can grow upon heat treatment in both types of alloys is very important for the discussion of the emissivity data that is introduced later on.
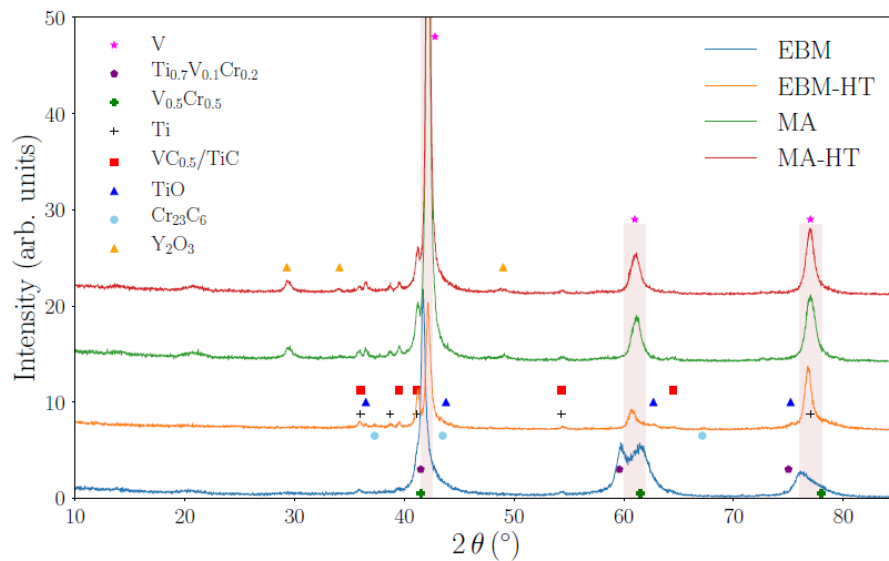
Figure 2 X-ray diffraction patterns obtained at room-temperature of all four samples. The indexation of the reflections shows the presence of different compositions in each sample.

## 3.2 Characterization of the outermost oxygen-rich layer

Efforts were made to reduce oxidation as much as possible, due to the oxygen affinity and solubility of vanadium. However, a very slight oxidation was observed after the emissivity measurements in all four samples. In order to analyze the potential influence of this surface oxidation on the emissivity data, the oxide layer was characterized by different techniques. XRD patterns were acquired at small glancing angles (2, 5, 10, 15 and 50º with respect to the sample surface) with the purpose of enhancing the

contribution of the outermost oxide layer, but no different reflections with respect to those observed in the Bragg-Brentano geometry used for the patterns shown in Figure 2 were observed. This rules out the possibility of a thick oxide layer. Then, taking advantage of the presence of a region that had not been in contact with the atmosphere (a masked area at the corner of the sample) and using atomic force microscopy, it was observed that there was no step at the boundary between the oxidized area and the metallic area. This is consistent with an internal mode of oxidation.

Finally, to determine the thickness of the layer, X-ray Photoelectron Spectroscopy (XPS) depth profiles were acquired in both areas. Figure 3 shows a semi-quantitative estimation of the ratio between the signals corresponding to V, Ti and O (only these signals were integrated to calculate the percentage). Other minority elements such as Cr, N and C were also detected, but were not relevant for the determination of the thickness of the oxide layer. The metallic area (continuous lines) showed a native oxide layer of 5 nm and an oxygen penetration layer of 20 nm approximately. After 25 nm the content of oxygen remains constant and it is representative of the oxygen concentration in the bulk. On the other hand, the region that had been in contact with the atmosphere (dashed lines), shows an oxide layer of around 15 nm and an oxygen penetration layer of 125 nm. Beyond 140 nm the oxygen content is also the same as in the bulk as seen in the measurement in the metallic area. In addition, when analyzing the XPS spectra corresponding to V and Ti, it is clearly observed that they change from V (III) and Ti (IV) in the oxide layer to metallic V and Ti in the bulk (Figure 4). It is also clearly detected how the O signal is significantly lower in the metallic area and decreases with increasing depth. Furthermore, the V and Ti signals shift from binding energies usually attributed to V (III) (around 515-516 eV) and Ti (IV) (458-459 eV) towards those corresponding to V (0) (about 512-513 eV) and Ti (0) (454 eV) respectively.

To summarize, when characterizing the outermost oxygen-rich layer formed during the emissivity measurements, it can be concluded that two layers are formed: a first oxide layer of about 15 nm, mainly consisting of V and Ti oxides. Although the Ti content in the alloy is small, due to its higher affinity with oxygen than that of V, surface segregation of Ti was observed for the same alloy at similar conditions [30].This leads to a detectable amount of stable TiO_2 in addition to V oxide in this first layer. The second zone is an oxygen penetration layer of about 125 nm. The thickness of the whole oxide layer is below the limit after which it can have significant effects on the

emissivity data, since the thickness (15 nm) is between 2 and 3 orders of magnitude lower than the measured radiation wavelengths.
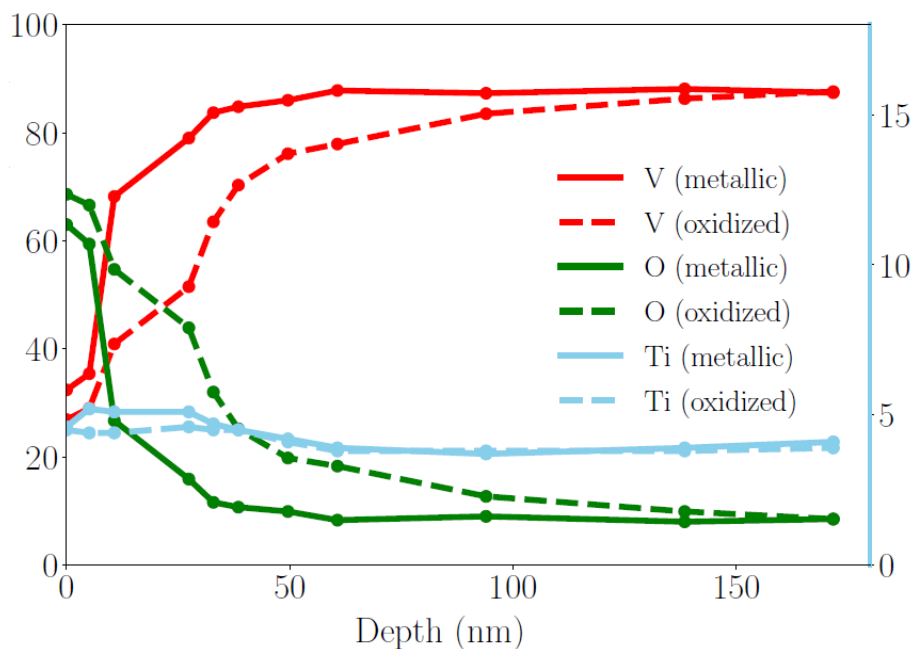
Figure 3. X-ray photoelectron spectroscopy (XPS) depth profiles for a metallic surface (continous lines) and a surface exposed to the atmosphere (dashed lines) of vanadium (red), titanium (sky blue) and oxygen (green) relative content. Ar+ sputtering with 3000 and 5000-eV ion energies and a 10-mA current was applied.
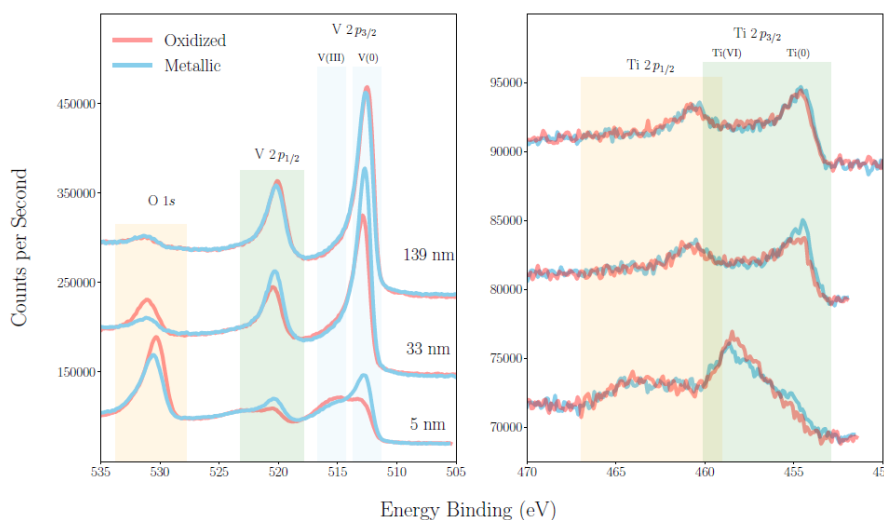

Figure 4 XPS spectra acquired at different depth in the oxidized area (red) and the metallic region (blue). It is clearly observed how the O signal is significantly lower in the metallic area and decreases with increasing depth. In addition, it is observed that the V $2p_{3/2}$ signal shifts from binding energies usually attributed to V (III) (around 515-516 eV) towards those corresponding to V (0) (about 512-513 eV). On the right, the scale was changed to clearly show the Ti $2p_{3/2}$ signal shift from 458-459 eV typical for Ti (IV) towards that of metallic Ti (0) (about 554 eV).

3.3 Emissivity measurements

Two thermal cycles were performed in the HAIRL radiometer in each of the four samples between 200 and 750 ºC. In the first cycle, possible surface tensions created during polishing were eliminated [31]. Once the surface tensions were relaxed, a systematic emissivity study was performed from 10 to 80º and between 3 and 22 μm. The temperature-dependent normal spectral emissivity is shown in Figure 5 (data is not corrected from residual water and CO_2 IR absorption peaks from the blackbody spectrum). In this figure and thereafter, the shades correspond to the expanded uncertainty (k=2). The emissivity curves show the typical metallic behavior with low emissivity values that increase with temperature and decrease with wavelength [31]. As it can be seen from the evolution of the emissivity for both HT samples, the MA-HT alloy presents weaker temperature dependence than the EBM-HT one, which can be associated with the stability of the microstructure. This would indicate that, similar to what has been measured for other properties (e.g. mechanical), the radiative properties of this improved V-based alloys are more stable than those of the original alloys [21-23].
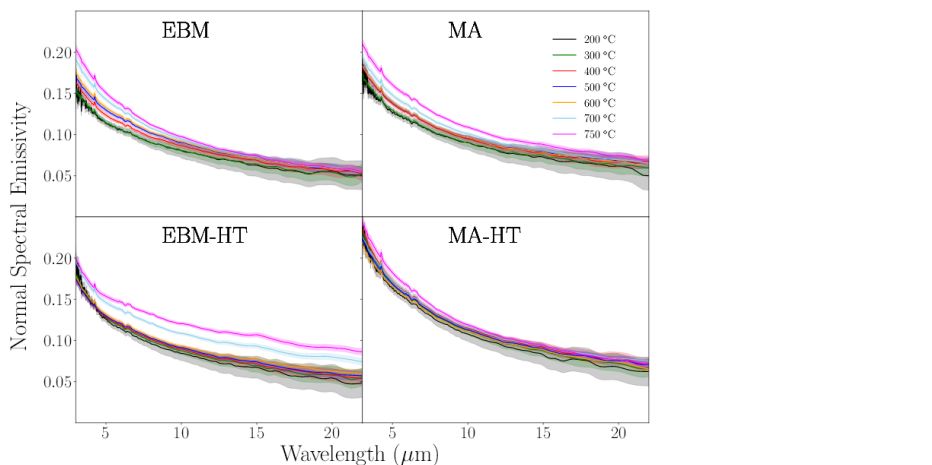

Figure 5 Temperature-dependent normal spectral emissivity measurements for the four samples between 200 and 750 ºC.

Figure 6 shows a comparison between normal spectral emissivity measurements of treated and untreated samples for each alloy at low (200 ºC) and high (700 ºC) temperatures. This reveals that heat treatment increases the normal spectral emissivity in both sets of samples and that MA & MA-HT samples have a larger normal spectral emissivity than EBM & EBM-HT samples, respectively. However, two different types of emissivity increase can be observed in Figure 6. On the one hand, the emissivity increases more at short wavelengths than at long ones for both MA samples at high and low temperatures and for both EBM samples only at low temperature. On the other hand, the EBM-HT has the same emissivity as EBM at short wavelengths, while at longer ones it is clearly higher.

Besides, Figure 7 shows directional spectral emissivity measurements at 700 °C for all four samples. Similar to what is observed in Figure 6, the biggest evolution between EBM and EBM-HT samples at short angles occurs more at long wavelengths than at short ones. However, from 50° onwards, the EBM-HT spectra become parallel to the EBM spectra. MA and MA-HT samples also show the same type of behavior as in Figure 6 at small angles, where the emissivity increases more at shorter wavelengths, but at 70 and 80° both curves are parallel. Additionally, when comparing both untreated samples, it can be seen that their directional emissivities do not show strong differences except at 60°. In the case of the treated samples, the EBM-HT emissivity is higher than the MA-HT one at all angles except at 10°.

In order to explain the differences between the measured emissivity curves, knowledge of the microstructure is necessary. The microstructural analysis reported above and the ones performed in previous works [21,22] have concluded that changes in several physical properties can be attributed to microstructural evolution: grain growth of secondary phases (Ti/Cr-carbides and/or oxides), increase of the size and concentration of precipitates or a take-up of residual interstitials from the imperfect vacuum; as well as intrinsic evolution of the (V) matrix itself. The observed evolution of the emissivity with heat treatment suggests that these microstructural changes may also have an effect on the optical and radiative properties of these materials. This evolution can be explained by two different mechanisms, depending on the spectral range at which they take place. In the long-wavelength limit, the optical properties of metals are described by the Hagen-Rubens equation, which is proportional to the electrical resistivity [32]. The evolution of the main phase, evidenced by observed mechanical instability [22] and consistent with an increase in the resistivity in the EBM-HT sample, can therefore explain such evolution at long wavelengths. However, differences in the short wavelength region can be described by an effective medium theory. For example, the Maxwell-Garnett model describes the material as a matrix with embedded particles corresponding to the secondary phases, which are assumed to be small and spherical [33]. In the case of these alloys, the matrix corresponds to an electrically conducting material that can be described by the Drude model [34], while the secondary phases are dielectric. Given this structure, the model predicts an increase in the emissivity in the near-infrared and no significant changes at longer wavelengths. Therefore, it is shown that it is necessary to understand the relationship between the microstructure and the spectral emissivity to be able to properly characterize changes in the thermal radiative properties of alloys.
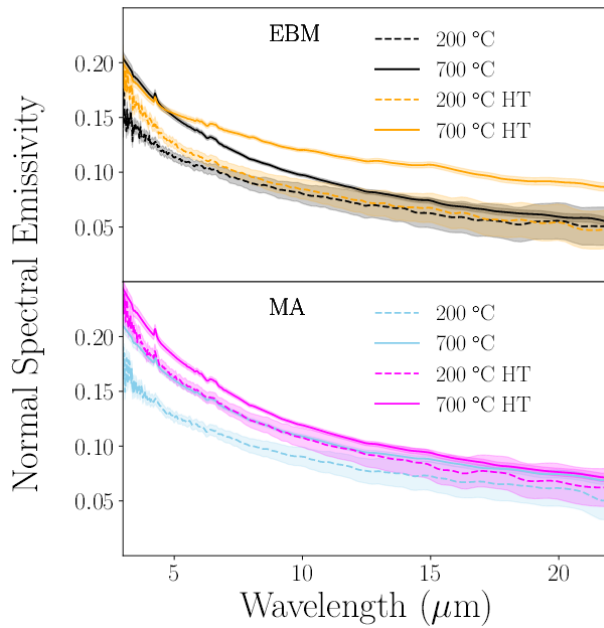
Figure 6 Normal spectral emissivity measurements for both alloys with (continuous) and without (dashed) annealing at low (200 ºC) and high (700 ºC) temperatures.
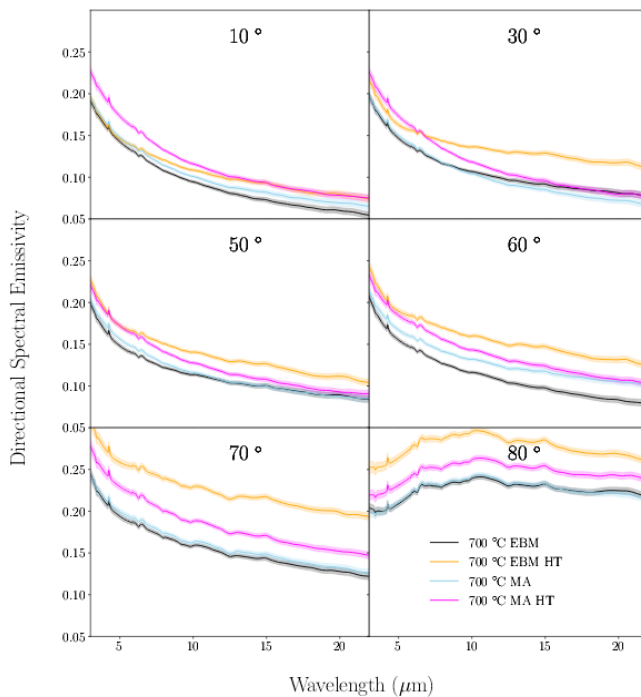
Figure 7 Directional spectral emissivity measurements at 700 ºC for all samples at different angles.

The directional spectral emissivity measurements at 700 ºC between 10º and 80º are presented in Figure 8 to further analyze the details. Figure 8 shows the directional spectral emissivity of the EBM sample at 3 different wavelengths. It is evident that this alloy follows the typical metallic behavior, where the emissivity slightly varies at low angles up until 50º, increases up more rapidly until it reaches a maximum between 70-

85º and then drops down to 0 at 90º, as forced by electromagnetic boundary conditions. The lines connecting the dots are made by a spline and only help showing where these emissivity maxima might be situated. Once again, it can be seen that the heat treatment induces an emissivity increase at all angles and wavelengths for both compositions, although it does not change the metallic behavior of the directional emissivity.
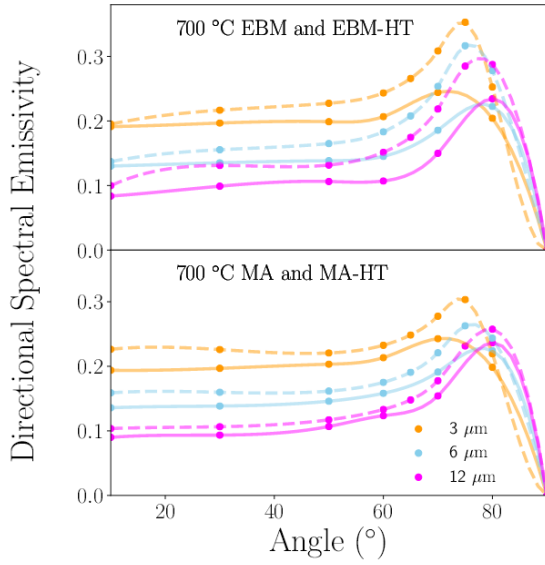

Figure 8 Spectral emissivity evolution with the angle at 700 ºC at 3 different wavelengths for all 4 samples. Continuous lines refer to pre-annealed alloys, whereas dashed lines refer to post-annealed alloys.

Finally, the spectral directional results were integrated in order to obtain the total hemispherical emissivity, which is the key parameter for heat transfer calculations. The procedure used is similar to the one followed by other authors for calculation based on radiometric methods [35,36], and has been validated as a viable alternative to the conventional calorimetric methods to calculate the total hemispherical emissivity [37]. Radiometric methods rely on a more complex approach to the calculation of this property, but they can be measured in the same instrument as the spectral emissivity, which constitutes a great practical advantage.

The directional spectral emissivity at each temperature was numerically integrated in both solid angle and wavelength with a Planck function weighing factor, as shown in the Equation 1. The convenient extrapolation procedures for wavelengths outside of the measured spectral range are explained elsewhere [38].

$$\varepsilon_H(T) = \frac{1}{\pi} \int_0^{2\pi} \int_0^{\frac{\pi}{2}} \frac{\int_0^\infty \varepsilon(\lambda, \theta, T) L(\lambda, T) d\lambda}{\int_0^\infty L(\lambda, T) d\lambda} cos\theta sin\theta d\theta d\phi \qquad (1)$$

The results are shown in Figure 9. The total hemispherical emissivity values increase with temperature, as metallic materials usually do. This is due to the increase of the spectral emissivity with temperature and the Planck function ($L(\lambda, T)$) maximum shift towards shorter wavelengths, where the emissivity of the metallic materials is higher. No data for these alloys is available for comparison, but electrical resistivity data of V-4Cr-4Ti between 400 and 600 ºC obtained in Ref. [39] is used to calculate the total hemispherical emissivity using the Davisson-Weeks equation, as modified by Parker and Abbott [32]. The obtained values are depicted in red dots and the extrapolated dashed line is obtained by doing a linear fit on the electrical resistivity data. They show a really good agreement with the emissivity data from this work as they lie between the EBM and EBM-HT hemispherical emissivity values. Finally, it is clearly seen that both set of samples present a higher total hemispherical emissivity when the heat treatment is performed. This means that the heat treatment enhances the emissivity of the alloys; this increase in the total hemispherical emissivity translates into a larger radiative heat transfer efficiency.
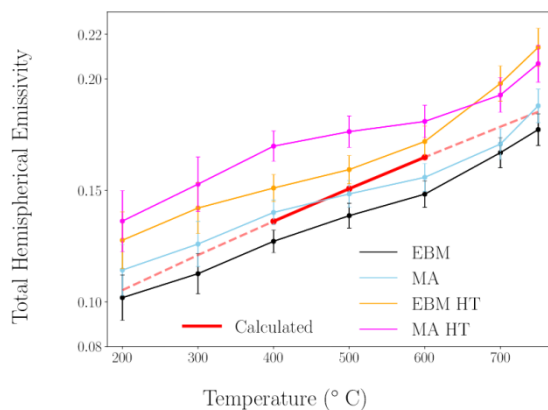
Figure 9 Total hemispherical emissivity for all four samples between 200 and 750 ºC. The red dots are obtained calculating the total hemispherical emissivity through electrical resistivity measurements made in a V-4Cr-4Ti in Ref [39].

4 Conclusions

The spectral directional emissivity of two alloys of the V-Cr-Ti family with and without a heat treatment between 200 ºC and the working temperatures of fusion reactors (700-750 ºC) has been studied. Emissivity measurements show that heat treatment increases the emissivity for both compositions. XPS shows that the oxide layer formed during measurements is of 15 nm, below the necessary thickness in order to significantly affect the emissivity curves. Nevertheless, SEM, TEM and XRD analysis show coarsening of secondary phases and precipitates and a take-up of residual interstitials from the imperfect vacuum, which lead to increases in the emissivity. These

increases have been related to different physical mechanisms, depending on the spectral region. The total hemispherical emissivity is also obtained by integrating the directional spectral emissivity curves along the electromagnetic spectrum and the solid angle. The obtained values are in agreement with total hemispherical emissivity data calculated from existing electrical resistivity data. Besides, the increase on the total hemispherical emissivity when the heat treatment is performed entails an improvement on the thermal radiative properties of these alloys, since they possess a higher self-refrigerating capability. Overall, these data are crucial thermophysical parameters for calculations of heat flow and temperature measurement inside the reactor, and thus this work fills a deficiency on the thermophysical characterization of structural materials for the fusion reactors.

Acknowledgements

Data Availability

Data will be available upon request.

References

[1] T. Muroga, J. Chen, V. Chernov, R. Kurtz, M. L. Flem, Present status of vanadium alloys for fusion applications, Journal of Nuclear Materials 455 (2014) 263–268. http://dx.doi.org/10.1016/j.jnucmat.2014.06.025.

[2] T. Muroga. Structural Materials for Generation IV Nuclear Reactors, Refractory metals as core materials for Generation IV nuclear reactors, Pages 415-440. Elsevier, Amsterdam, 2017.

[3] M. Le Flem, J.M. Gentzbittel, P. Wident, Assessment of a European V-4Cr-4Ti alloy – CEA-J57, Journal of Nuclear Materials 442 (1) (2013) 325-329. http://dx.doi.org/10.1016/j.jnucmat.2013.02.072

[4] J. Chen, V. Chernov, R. Kurtz, T. Muroga, Overview of the vanadium alloy researches for fusion reactors, Journal of Nuclear Materials 417 (2011) 289–294. http://dx.doi.org/10.1016/j.jnucmat.2011.02.015.

[5] S.J. Zinkle, H. Matsui, D.L. Smith, A.L. Rowcliffe, E. van Osch, K. Abe, V.A. Kazakov, Research and development on vanadium alloys for fusion applications, Journal Nuclear Materials 258-263 (1998) 205-214. http://dx.doi.org/10.1016/S0022-3115(98)00269-4.

[6] A. Raffray, M. Akiba, V. Chuyanov, L. Giancarli, S. Malang, Breeding blanket concepts for fusion and materials requirements, Journal of Nuclear Materials 307311, Part 1 (2002) 21–30. http://dx.doi.org/10.1016/S0022-3115(02)01174-1.

[7] F. Lott, A. Netchaieff, F. Escourbiac, J.-L. Jouvelot, S. Constans, D. Hernandez, Advances in optical thermometry for the ITER divertor, Fusion Engineering and Design 85 (2010) 146–152. http://dx.doi.org/10.1016/j.fusengdes.2009.08.007.

[8] D. Hernandez, J. Badie, F. Escourbiac, R. Reichle, Development of two-colour pyroreflectometry technique for temperature monitoring of tungsten plasma facing components, Fusion Engineering and Design 83 (2008) 672–679. http://dx.doi.org/10.1016/j. fusengdes.2008.02.008.

[9] Y. Seki, K. Ezato, S. Suzuki, K. Yokoyama, M. Enoeda, S. Mori, Non-destructive examination with infrared thermography system for ITER divertor components, Fusion Engineering and Design 85 (2010) 1451–1454. http://dx.doi.org/10.1016/j.fusengdes.2010.04.010.

[10] Y. Zhang, Y. Zhang, R.Lu, S. Shu, X. Lang, L. Yang, Investigation of the normal spectral band emissivity characteristic within 7.5 to 13 μm for Molybdenum between 100 and 500 °C, Infrared Physics and Technology 88 (2018) 74-80. http://dx.doi.org/10.1016/j.infrared.2017.11.017.

[11] G. Cao, S. Weber, S. Martin, M. Anderson, K. Sridharan, T. Allen, Spectral emissivity measurements of candidate materials for very high temperature reactors, Nuclear Engineering and Design 251 (2012) 78–83. http://dx.doi.org/10.1016/j.nucengdes.2011.10.067.

[12] C. Ruset, D. Falie, E. Grigore, M. Gherendi, V. Zoita, K.-D. Zastrow, G. Matthews, X. Courtois, J. Bucalossi, J. Likonen, The emissivity of W coatings deposited on carbon materials for fusion applications, Fusion Engineering and Design 114 (2017) 192–195. http://dx.doi.org/10.1016/j.fusengdes.2016.12.015.

[13] B. P. Keller, S. E. Nelson, K. L. Walton, T. K. Ghosh, R. V. Tompson, S. K. Loyalka, Total hemispherical emissivity of Inconel 718, Nuclear Engineering and Design 287 (2015) 11–18. http://dx.doi.org/10.1016/j.nucengdes.2015.02.018.

[14] T. S. Hunnewell, K. L. Walton, S. Sharma, T. K. Ghosh, R. V. Tompson, D. S. Viswanath, S. K. Loyalka, Total hemispherical emissivity of SS 316L with simulated very high temperature reactor surface conditions, Nuclear Technology 198 (2017) 293–305. http://dx.doi.org/10.1080/00295450.2017.1311120.

[15] A. Stanimirovic, G. Vukovic, K. Maglic, Thermophysical and thermal optical properties of vanadium by millisecond calorimetry between 300 and 1900 K, International Journal of Thermophysics 20 (1999) 325–332. http://dx.doi.org/10.1023/A:1021471423350.

[16] G. Pottlacher, T. Hopf, B. Wilthan, C. Cagran, Thermophysical data of liquid vanadium, Thermochimica Acta 461 (2007) 88–95. http://dx.doi.org/10.1016/j.tca.2006.12.010.

[17] P.-F. Paradis, T. Ishikawa, T. Aoyama, S. Yoda, Thermophysical properties of vanadium at high temperature measured with an electrostatic levitation furnace, The Journal of Chemical Thermodynamics 34 (2002) 1929–1942. http://dx.doi.org/10.1016/S0021-9614(02)00126-X.

[18] S. X. Cheng, P. Cebe, L. M. Hanssen, D. M. Riffe, A. J. Sievers, Hemispherical emissivity of V, Nb, Ta, Mo, and W from 300 to 1000 K, Journal of the Optical Society of America B 4 (1987) 351–356. http://dx.doi.org/10.1364/JOSAB.4.000351.

[19] C. R. Roger, S. H. Yen, and K. G. Ramanathan, Temperature variation of total hemispherical emissivity of stainless steel AISI 304, Journal of the Optical Society of America 69 (1979) 1384-1390. http://dx.doi.org/10.1364/JOSA.69.001384.

[20] T. Makino and T. Kunitomo, Dispersions of Optical Constants and Emissivities of Iron and Steel in the Temperature Range up to the Curie Point, Bulletin of JSME 20 (1977) 1607-1614. http://dx.doi.org/10.1299/jsme1958.20.1607.

[21] B. P. Wynne, M. Gorley, P.F. Zheng A. Cackett, M. Porton, E. Surrey, An analysis of the microstructure of spark plasma sintered and hot isostatically pressed V-4Cr-4Ti-1.8Y-0.4Ti$_3$SiC$_2$ alloy and its thermal stability, Journal of Alloys Compounds, 680 (2016) 506-511, 2016. http://dx.doi.org/10.1016/j.jallcom.2016.04.159.

[22] H.Y. Fu, J.M. Chen, P.F. Zheng, T. Nagasaka, T. Muroga, Z.D. Li, S. Cui, Z.Y. Xu, Fabrication using electron beam melting of a V–4Cr–4Ti alloy and its thermo-mechanical strengthening study, Journal of Nuclear Materials 442 (2013) S336–S340. http://dx.doi.org/10.1016/j.jnucmat.2013.01.337.

[23] P. Zheng, T. Nagasaka, T. Muroga, J. Chen, Microstructures and mechanical properties of mechanically alloyed V-4Cr-4Ti alloy dispersion strengthened by nano-

particles, Fusion Engineering and Design 89 (2014) 1648–1652. http://dx.doi.org/10.1016/j.fusengdes.2014.03.020.

[24] L. del Campo, R.B. Pérez-Sáez, X. Esquisabel, I. Fernández, M.J. Tello, New experimental device for infrared spectral directional emissivity measurements in a controlled environment, Review of Scientific Instruments 77 (2006) 133111. http://dx.doi.org/10.1063/1.2393157.

[25] R.B. Pérez-Sáez, L. del Campo, M.J. Tello, Analysis of the accuracy of the methods for the direct measurement of emissivity, International Journal of Thermophysics 29 (2008) 1141-1155. http://dx.doi.org/10.1007/s10765-008-0402-4.

[26] L. González-Fernández, R.B. Pérez-Sáez, L. del Campo, M.J. Tello, Analysis of calibration methods for direct emissivity measurements, Applied Optics 49 (2010) 2728-2735. http://dx.doi.org/10.1364/AO.49.002728.

[27] T. Echániz, R.B. Pérez-Sáez, M.J. Tello, IR radiometer sensitivity and accuracy improvement by eliminating spurious radiation for emissivity measurements on highly specular samples in the 2–25 μm spectral range, Measurement 110 (2017) 22-26. http://dx.doi.org/10.1016/j.measurement.2017.06.010.

[28] L. del Campo, R.B. Pérez-Sáez, L. González-Fernández, M.J. Tello, Combined standard uncertainty in direct emissivity measurements, Journal of Applied Physics 107 (2010) 113510. http://dx.doi.org/10.1063/1.3431541.

[29] K. Natesan, M. Uz, Oxidation performance of V-Cr-Ti alloys, Fusion Engineering and Design 51-52 (2000) 145–152. http://dx.doi.org/10.1016/S0920-3796(00)00308-2.

[30] Y. Atano, R. Ayakawa, K. Nishino, S. Ikeno, T. Nagasaka, T. Muroga, K. Watanabe, Surface segregation of Ti in a V-4Cr-4Ti alloy and its influence on the surface reaction rates of hydrogen isotopes, Materials Transactions 46 (2005) 511-516. https://doi.org/10.2320/matertrans.46.511.

[31] I. Setién-Fernández, T. Echániz, L. González Fernández, R.B. Pérez Sáez, M.J. Tello. Spectral emissivity of copper and nickel in the mid-infrared range between 250 and 900 ºC, Journal of Heat and Mass Transfer 71 (2014) 549-554. http://dx.doi.org/10.1016/j.ijheatmasstransfer.2013.12.063.

[32] A.J. Sievers, Thermal radiation from surface metals, Journal of the Optical Society of America 68 (1978) 1505-1516. http://dx.doi.org/10.1364/JOSA.68.001505.

[33] M. Wang, N. Pan, Predictions of effective physical properties of complex multiphase materials, Materials Science and Engineering R: Reports 63 (2008) 1-30. http://dx.doi.org/10.1016/j.mser.2008.07.001.

[34] A.D. Rakić, A.B. Djurišić, J.M. Elazar, and M.L. Majewski, Optical properties of metallic films for vertical-cavity optoelectronic devices, Appl. Opt. 37 (1998) 5271-5283. https://doi.org/10.1364/AO.37.005271

[35] A. Adibekyan, C. Monte, M. Kehrt, B. Gutschwager, J. Hollandt, Emissivity measurement under vacuum form 4 μm to 100 μm and from 40 ºC to 450 ºC at PTB, International Journal of Thermophysics 36 (2015) 283-289. http://dx.doi.org/10.1007/s10765-014-1745-7.

[36] M. Balat-Pichelin, J. Sans, E. Beche, V. Flaud, J. Annaloro, Oxidation and emissivity of Inconel 718 alloy as potential space debris during its atmospheric entry, Materials Characterization 17 (2017) 379-390. https://doi.org/10.1016/j.matchar.2017.02.016.

[37] J.-P. Monchau, J. Hameury, P. Ausset, B. Hay, L. Ibos, Y. Candau, Comparative study of radiometric and calorimetric methods for total hemispherical emissivity measurements, Heat and Mass Transfer 54 (2018) 1415-1425. http://dx.doi.org/10.1007/s00231-017-2238-6.

[38] I. Setién-Fernández, T. Echániz, L. González-Fernández, R.B.Pérez-Sáez, E. Céspedes, J.A: Sánchez-García, L. Pérez-Fraga, R. Escobar Galindo, J.M. Albella, C. Prieto, M.J. Tello, First spectral emissivity study of a solar selective coating in the 150-600 ºC temperature, Solar Energy Materials & Solar Cells 117 (2013) 390-395. http://dx.doi.org/10.1016/j.solmat.2013.07.002.

[39] D.L. Smith, H.M. Chung, B.A. Loomis, H. Matsui, S. Votinov, W. Van Witzenburg, Development of vanadium-base alloys for fusion first-wall-blanket applications, Fusion Engineering and Design 29 (1995) 399-410. http://dx.doi.org/10.1016/0920-3796(95)80046-Z.